

# Growth process conditions of vertically aligned carbon nanotubes using plasma enhanced chemical vapor deposition

M. Chhowalla,<sup>a)</sup> K. B. K. Teo, C. Ducati, N. L. Rupesinghe, G. A. J. Amaratunga, A. C. Ferrari, D. Roy, J. Robertson, and W. I. Milne

*Engineering Department, University of Cambridge, Cambridge CB2 1PZ, United Kingdom*

(Received 5 March 2001; accepted for publication 13 August 2001)

The growth of vertically aligned carbon nanotubes using a direct current plasma enhanced chemical vapor deposition system is reported. The growth properties are studied as a function of the Ni catalyst layer thickness, bias voltage, deposition temperature,  $C_2H_2:NH_3$  ratio, and pressure. It was found that the diameter, growth rate, and areal density of the nanotubes are controlled by the initial thickness of the catalyst layer. The alignment of the nanotubes depends on the electric field. Our results indicate that the growth occurs by diffusion of carbon through the Ni catalyst particle, which rides on the top of the growing tube. © 2001 American Institute of Physics.

[DOI: 10.1063/1.1410322]

## I. INTRODUCTION

Carbon nanotubes are attracting great interest for their remarkable properties such as ballistic electron transport and large elastic moduli. The high surface area and chemical inertness of nanotubes grown directly onto desired substrates makes them attractive for demanding applications such as electrochemistry, electrodes for fuel cells and supercapacitors.<sup>1–6</sup>

High quality single walled carbon nanotubes (SWNTs) and multiwalled carbon nanotubes (MWNTs) can be obtained using high pressure arcs, laser ablation, and high pressure chemical vapor deposition (CVD).<sup>7–12</sup> Many applications desire nanotubes with well defined diameters and lengths. MWNTs can be deposited using plasma enhanced chemical vapor deposition (PECVD) methods onto substrates coated with a suitable transition metal catalyst.<sup>13–19</sup> The essential parameters involved in the growth of vertically aligned carbon nanotubes (VACNTs) are the feed gas, the nature of the catalyst, and the substrate temperature. Free standing aligned nanotubes were first grown using a hot filament plasma enhanced chemical vapor deposition method.<sup>14</sup> Subsequently, various plasma methods have been used.<sup>16–20</sup>

There is presently great interest in VACNTs for field emission and vacuum microelectronic devices because carbon nanotubes are among the best field emitters presently available.<sup>21–25</sup> Their excellent field emission characteristics are attributed to the high aspect ratios, resulting in a large field enhancement factor. Carbon nanotubes are also mechanically and chemically robust and can emit large current densities at low electric fields.<sup>24</sup> The ability to grow carbon nanotubes on conducting substrates over a large area is essential for uniform emission required for vacuum microelectronic devices.

In this article, we report on the growth of vertically aligned nanotubes using a direct current (dc) glow discharge CVD system and a Ni or Co catalyst. We have performed a

detailed parametric study of the various factors influencing the growth of aligned carbon nanotubes. Specifically, we investigated the effects of catalyst layer thickness, the applied bias voltage, the deposition temperature, and the  $C_2H_2:NH_3$  gas flow ratio on the nanotube growth rate, diameter, density, and structure. It is believed that the nanotubes grow by the decomposition of the carbonaceous gas on the surface of a catalyst particle. The carbon dissolves in the catalyst, diffuses through it, and exits to form the nanotube. The role of the  $NH_3$  is to etch by-products such as amorphous carbon. Our process consists of four stages; substrate pretreatment, catalyst deposition, catalyst annealing (sintering), and then nanotube growth. The initial catalyst layer is formed into nanoparticles or islands by annealing or sintering at high temperature. This sintering depends on the annealing temperature and also on the interaction of the catalyst layer with the substrate. Therefore the initial condition of the substrate is important and we define it in a pretreatment step. The nanotubes are then characterized using scanning electron microscopy (SEM), high-resolution transmission electron microscopy (HREM), Raman spectroscopy and Auger spectroscopy. The results show that the catalyst thickness is important in controlling the nanotube diameter, length, and density, and their alignment is controlled by the electric field. Deposition temperature and plasma characteristics are also important for the growth of uniform, well-aligned nanotubes with few defects.

## II. EXPERIMENTAL DETAILS

The VACNTs were grown using a direct current (dc) PECVD system on a resistively heated graphite substrate stage capable of reaching a maximum temperature of 1000 °C. The Si substrates were treated in several ways prior to the catalyst deposition. Untreated Si substrates with a thin native oxide, pristine Si [cleaned with hydrofluoric (HF) acid], and Si with a layer of 50 nm  $SiO_2$  grown using electron cyclotron resonance (ECR) were used as the substrates.

<sup>a)</sup>Electronic mail: mc209@eng.cam.ac.uk

Thin films (0.5–20 nm) of Co or Ni catalyst are then deposited onto the Si substrates using magnetron sputtering or thermal evaporation.

After depositing the catalyst layer, the substrates are transferred in air to the growth chamber. The bell jar chamber is pumped down to a base pressure of  $10^{-2}$  Torr using a rotary pump. 20–30 Torr of high purity hydrogen or nitrogen is then introduced via a leak valve. The samples were also annealed in vacuum in some cases. The substrates were heated to 750 °C and held at this temperature for 15 min to sinter the catalyst layer, with the plasma off, prior to initiating the deposition. The substrate temperature is measured by attaching a thermocouple directly to the graphite heater. After the treatment step, the chamber was evacuated to base pressure and ammonia ( $\text{NH}_3$ ) was introduced immediately. The  $\text{NH}_3$  flow was maintained by mass flow controllers at 200 sccm, achieving a pressure of 3.5 Torr.

A dc discharge between the cathode (sample) and the anode (2 mm diameter by 1 cm length copper wire) was initiated using an AE MDX 1 kW supply. The anode–cathode distance was 2 cm. The bias voltage ( $V_b$ ) was increased to –600 V and the acetylene ( $\text{C}_2\text{H}_2$ ) feed gas was introduced within a few seconds using a separate mass flow controller. The  $\text{C}_2\text{H}_2$  flow ratio was varied from 0 to 75% to investigate the effect of the  $\text{C}_2\text{H}_2:\text{NH}_3$  ratio on growth. The total pressure after introducing  $\text{C}_2\text{H}_2$  depends on the ratio used. The depositions were carried out for 15 min in a stable discharge.

The SEM studies were performed on a Hitachi S800-FE SEM operated at 20 kV. The HREM was performed on a JEOL 4000EX operated at 400 kV. The HREM samples were prepared by scraping the films off the substrates, dispersing them in an ethanol ultrasonic bath, and placing them onto copper grids. The Auger chemical analysis was carried out using a Physical Electronic PHI 680 Auger nanoprobe with a 10–15 nm electron beam probe with a multichannel plate detector. The structure of the nanotubes was studied by Raman spectroscopy. Unpolarized visible Raman spectra were obtained using a 514.5 nm Ar ion laser excitation and a Renishaw spectrometer. UV Raman spectra were recorded on a UV-enhanced charge coupled device camera on a different Renishaw spectrometer modified for use at 244 nm with fused silica optics. The UV Raman used the 244 nm line of an inter-cavity frequency-doubled Ar ion laser. The laser power was always less than  $0.5 \text{ mW}/\mu\text{m}^2$  to avoid sample damage. The spectral resolution was  $3 \text{ cm}^{-1}$ . In all cases, the spectra were obtained with the laser beam directed perpendicular to the samples and thus nominally parallel to the VACNTs.

### III. RESULTS

#### A. Influence of catalyst layer thickness

SEM observations of the Ni catalyst films after sputter deposition onto ECR  $\text{SiO}_2$  coated substrates showed that Ni films thicker than 1 nm were continuous with a few pinholes. Films thinner than 1 nm were found to be discontinuous in some regions. Figure 1 shows SEM photographs of Ni films of varying thickness after annealing. It is seen that the Ni

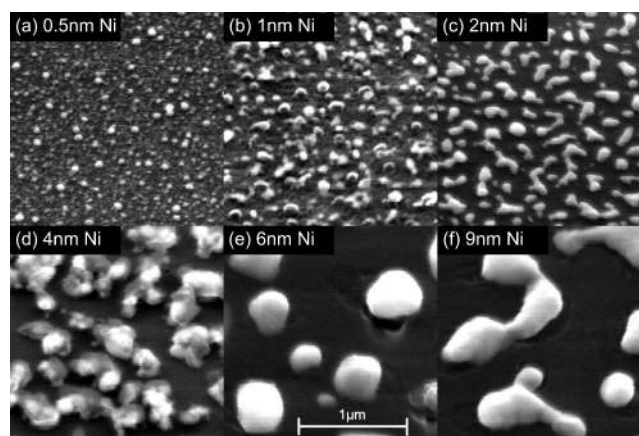


FIG. 1. SEM photographs of Ni films with varying thicknesses deposited using magnetron sputtering on 50 nm of ECR  $\text{SiO}_2$  after annealing at 750 °C in 20 Torr of  $\text{H}_2$  for 15 min.

breaks into small islands due to surface tension, as well as the compressive stress due to the mismatch of the thermal expansion coefficients of Si and Ni.<sup>16,17</sup>

The island size depends on the thickness of the initial Ni film, similar to the results of Bower *et al.*<sup>16</sup> Figure 2 shows that the average island size varies in proportion to the initial Ni layer thickness. The island diameter is much larger than the thickness, indicating that the islands have a low aspect ratio.

In contrast to this, no islands form after annealing Ni films deposited on a Si surface cleaned with HF or with only native oxide. The lack of fragmentation of Ni films on Si surfaces is attributed to the diffusion of Ni into the Si, leading to the formation of a silicide,  $\text{NiSi}_x$ , above 300 °C.<sup>26</sup> Therefore a barrier layer such as  $\text{SiO}_2$  is required to prevent silicide formation when using Ni as a catalyst. To study other potential barrier materials we also deposited Ni onto 100 nm Ti and W barrier layers. Postannealing results of Ni films on metal layers showed poorer results. However, similar annealing experiments with Co deposited on HF dipped Si and on Si with native oxide revealed significantly different results. The Co was found to form spherical islands similar to those in Fig. 1 even on a pristine Si surface, as seen in Fig. 3. The corresponding nanotube growth on Co islands is shown in Fig. 3(b).

Figure 4 shows the nanotubes grown on annealed Ni layers of different initial thickness, with a  $\text{C}_2\text{H}_2:\text{NH}_3$  flow

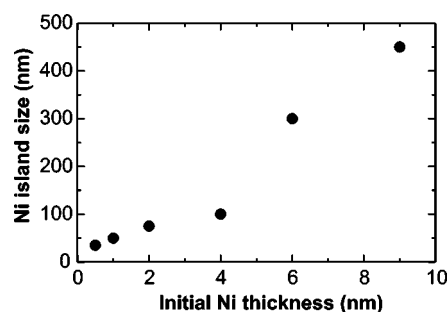


FIG. 2. The average Ni island size after annealing versus initial Ni layer thickness.

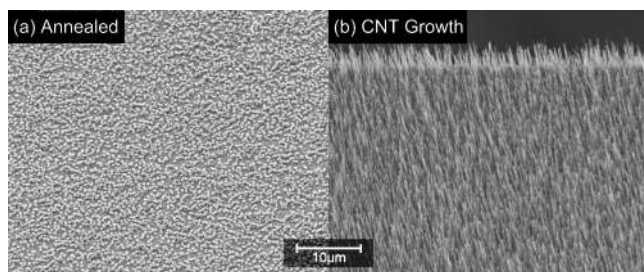


FIG. 3. (a) SEM photograph of a 2 nm magnetron sputtered Co film on HF cleaned Si after annealing in 20 Torr of  $H_2$  for 15 min. (b) Corresponding nanotube growth on Co particles.

ratio of 75:200 sccm at  $-600$  V and  $700^\circ\text{C}$ . All the results in Fig. 4 are for samples grown simultaneously in a single deposition. The thickness of the catalyst layer affects the tube diameter, the tube length, and the density of the tubes as seen in Fig. 5. Indeed, Fig. 6 shows that the nanotube diameter approximately equals the Ni island size.

In Fig. 4 a metal cap is observed predominantly at the top of the nanotubes for all our films grown using Ni or Co as the catalyst, as found by Ren *et al.*<sup>14</sup> and Merkulov *et al.*<sup>17</sup> but in contrast to Bower *et al.*<sup>16</sup> It can be seen that for catalyst thickness under 1.0 nm, the tubes are very thin and long with diameters as low as 10 nm and lengths up to  $10\ \mu\text{m}$ , similar to the results of Ren *et al.*<sup>14</sup> Figures 4(a) and 4(b) also show that the tubes are not perfectly aligned and appear distorted. As the catalyst layer thickness increases to 1.5–2.0 nm, the tubes become more uniform in diameter and are almost perfectly aligned. As the catalyst layer becomes even thicker, however, the average diameter and the distribution of nanotube diameter both increase and they become much shorter. It is also worth noting that we did not observe any nanotube growth in the absence of a catalyst. The wider size distribution of the nanotubes for thick catalyst layers is attributed to the nonuniform fragmentation of the catalyst layer during annealing.

In some reports, catalyst layers as thick as 15–20 nm were used to grow nanotubes.<sup>17</sup> To investigate the growth

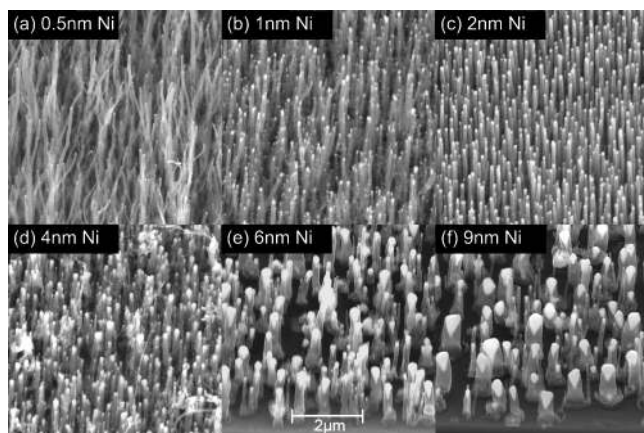


FIG. 4. SEM photographs of nanotubes grown on Ni layers of various initial thicknesses shown in Fig. 1. Standard growth conditions (bias voltage =  $-600$  V,  $C_2H_2:NH_3=75:200$ , time=15 min) were used for all depositions.

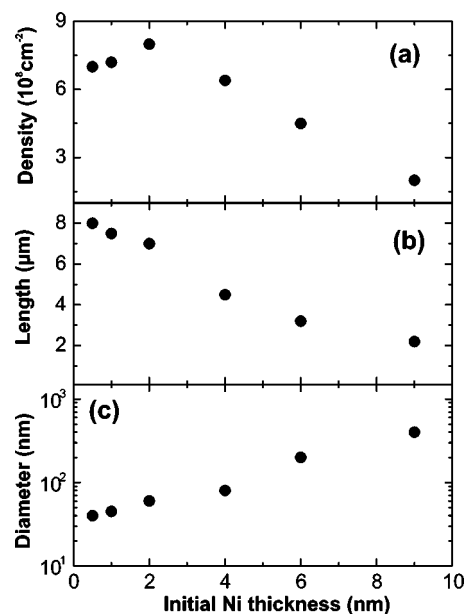


FIG. 5. Plot of average (a) nanotube density, (b) nanotube length, and (c) tube diameter as a function of the Ni thickness.

mechanism on such thick catalyst layers we attempted to grow nanotubes on a 20 nm Co layer. However, we find that thick catalyst films do not form islands. An additional  $NH_3$  etch for 15 s was required to fragment the thick catalyst layer. The etching was performed by initiating a  $NH_3$  plasma at  $-600$  V, similar to that in Refs. 14 and 17. After this annealing and etching treatment, the Co film was found to form islands comparable to Fig. 1(f), as shown in Fig. 7(a). It may be that during the  $NH_3$  etching, the polycrystalline Co film is preferentially etched at the grain boundaries. Figure 7(b) shows the corresponding nanotube growth for a 20 nm Co layer. The growth is now substantially different to any seen in Fig. 4. The nanotubes appear to grow preferentially at the edges of each island, resembling the grain boundary growth seen by Huang *et al.*<sup>27</sup> for nanotubes on thick (1 mm) Ni substrates. We attribute this type of growth to the fact that the Co at the island edge is thinner than in the island middle, allowing the carbon to diffuse through and form nanotubes. The middle of the island effectively behaves like a continuous film where no nanotube growth can occur.

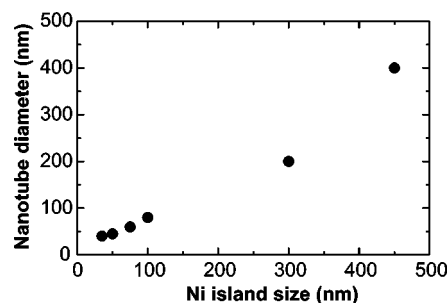


FIG. 6. The average nanotube diameter vs average Ni island size.



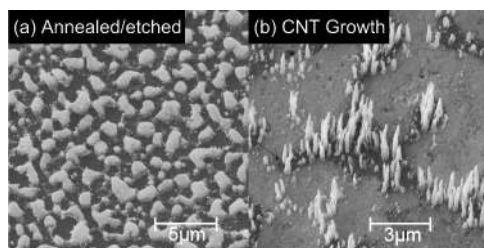


FIG. 7. (a) SEM photograph of a 20 nm Co film after annealing in  $H_2$  for 15 min and etching with  $NH_3$  (3.5 Torr) plasma for 15 s at  $-600V$ . (b) Corresponding nanotube growth on the 20 nm Co film using standard conditions.

## B. Plasma properties of dc PECVD

For dc plasmas, the glow discharge is initiated by applying a bias between the cathode and anode. The applied voltage governs the plasma properties if conditions such as electrode gap and pressure are kept constant. In order to understand the growth mechanism of the nanotubes some basic plasma parameters were measured using the graphite substrate holder as a planar Langmuir probe with an area of about  $10\text{ cm}^{-2}$ . The probe current is plotted against applied voltage in Fig. 8. The breakdown voltage for plasma initiation in our system is about  $-300\text{ V}$ , although this depends strongly on the substrate temperature. The plasma current density at  $-600\text{ V}$  was about  $9\text{ mA cm}^{-2}$ . The plasma potential ( $V_p$ ) obtained using a much smaller  $0.5\text{ mm} \times 0.5\text{ cm}$  tungsten wire probe was found to be  $3\text{ V}$ . The plasma density ( $n$ ) is derived from the current density to be  $10^{10}\text{ cm}^{-3}$ , taking the ion energy as 30% of the bias voltage or  $200\text{ eV}$ .

The electron temperature ( $T_e$ ) derived from the probe measurement was found to be  $1.5\text{ eV}$ . The Debye length,  $\lambda_d = (\epsilon_0 T_e / ne^2)^{1/2}$ , of the plasma was derived from these data as  $\approx 50\text{--}90\text{ }\mu\text{m}$ . The sheath width  $\sigma$  over which the bias voltage  $V_d$  is dropped is calculated from  $\lambda_d$  as<sup>28</sup>

$$\sigma = 0.47\lambda_d \left( \frac{2e|V_p - V_d|}{kT_e} \right)^{3/4},$$

where  $k$  is the Boltzmann constant. This gives a sheath width of about  $4\text{--}6\text{ mm}$ . Therefore the field across the sheath at  $-600\text{ V}$  is  $\approx 0.1\text{--}0.15\text{ V}/\mu\text{m}$ , similar to that found by Bower *et al.*<sup>29</sup> Note that when the voltage is reduced to  $-400\text{ V}$  the field is only  $0.07\text{ V}/\mu\text{m}$ , which is not enough to completely align the nanotubes as shown later.

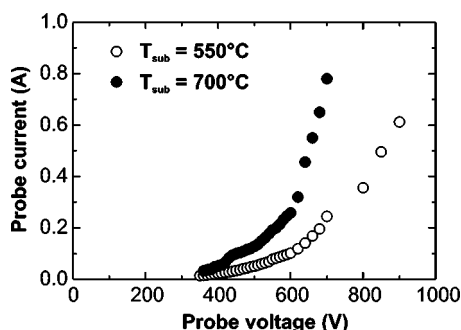


FIG. 8. Planar probe current versus the applied probe voltage characteristics taken at two different probe temperatures for the dc PECVD plasma used to grow aligned nanotubes.

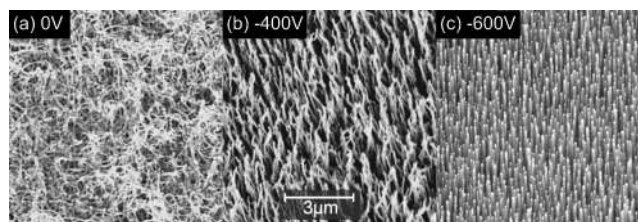


FIG. 9. SEM photographs of nanotubes grown at (a)  $0\text{ V}$ , (b)  $-400\text{ V}$ , and (c)  $-600\text{ V}$  for a Ni catalyst thickness of  $2\text{ nm}$ .

Returning to Fig. 8, it can be seen that the probe currents measured at  $750^\circ\text{C}$  are significantly higher than those at  $550^\circ\text{C}$ . This indicates that heating of the graphite substrate holder contributes to additional excitation of gas species in the plasma. The additional ionization may be due to collisions between neutral species and electrons in the sheath. The electrons may result from secondary emissions and/or field emitted electrons emanating from fine protrusions on the graphite surface. Therefore the higher growth rate and better quality nanotubes generally observed at higher temperatures may be partly due to the presence of specific excited or ionized  $C_2H_2^*$  and  $NH_3^*$  species rather than substrate temperature alone. The species required for nanotube growth is presently being studied and will be reported elsewhere.

## C. Influence of applied voltage

Figure 9 shows nanotubes grown at three different bias voltages while keeping all other parameters constant. At  $0\text{ V}$  bias, no plasma is present and the nanotubes grow only by thermal decomposition of  $C_2H_2$ . No electric field is present, and the nanotubes are randomly oriented or spaghetti-like, as shown in Fig. 9(a). If a small bias voltage is applied, a weak plasma is generated, a weak electric field is present above the substrate, and some alignment begins to occur as observed in Fig. 9(b). However, an electric field of about  $0.07\text{ V}/\mu\text{m}$  ( $-400\text{ V}$ ) does not appear to be enough to completely align the nanotubes. In contrast, nanotubes deposited at  $-600\text{ V}$  (electric field  $\approx 0.15\text{ V}/\mu\text{m}$ ) are perfectly aligned with uniform diameter and length. Although Fig. 9 indicates the effect of applied field on alignment, it must be noted that the plasma characteristics (such as the bias current, degree of ionization/excitation) at  $0$ ,  $-400$ , and  $-600\text{ V}$  are expected to be significantly different in terms of the types and amount of species contributing to growth. The changes in plasma characteristics may also contribute to the degree of alignment, though not for the nucleation of nanotubes.

Figure 10 shows the deposition rate as a function of the applied bias voltage. Here we use the deposition rate rather than the nanotube length, as thermally deposited tubes are not aligned and so it is difficult to estimate their length. Surprisingly, we found that the deposition rate decreases with increasing bias voltage. This rather unexpected result is attributed to greater etching by ionized or excited  $NH_3$  species. The  $NH_3$  etching is strongest when a plasma is initiated, as indicated by the sharp drop in the deposition rate when the bias voltage is above  $-300\text{ V}$ .  $NH_3$  etching is an important

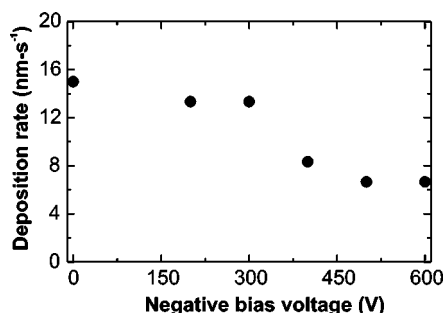


FIG. 10. Average deposition rate versus the applied bias voltage using a  $C_2H_2:NH_3$  ratio of 75:200 and Ni thickness of 2 nm.

aspect of growing well-aligned nanotubes with uniform diameters from top to bottom (see below).

Figure 11(a) shows the nanotube length (growth rate) as a function of the deposition time. We see that the length increases linearly with time, in contrast to the results of Bower *et al.*, who observe that the nanotube length saturates quickly after the first 3 min.<sup>16</sup> This result, together with the fact that the catalyst particle remains at the top of the nanotubes, indicates different growth mechanisms for the two cases.

Note that our nanotube lengths are significantly less than those of other groups.<sup>14,16,17,27</sup> This is due to the relatively low pressure (4 Torr compared to 20 Torr) used here. Figure 11(b) shows the nanotube length as a function of the total gas pressure, while keeping the  $C_2H_2:NH_3$  ratio constant. It is seen that the nanotube length increases with gas pressure.

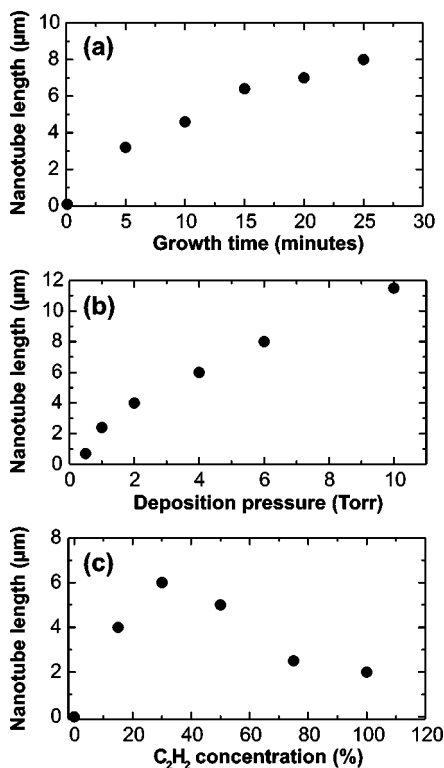


FIG. 11. Average nanotube length as a function of (a) growth time, (b) deposition pressure, and (c)  $C_2H_2$  concentration.

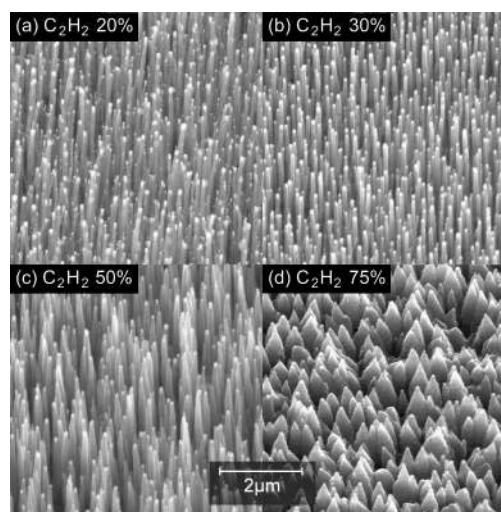


FIG. 12. SEM photographs of nanotubes grown at different concentrations of  $C_2H_2$ , (a) 20%, (b) 30%, (c) 50%, and (d) 75%. Note that the  $NH_3$  flow was kept constant at 100 sccm.

#### D. Influence of the $C_2H_2:NH_3$ ratio

Figure 12 shows micrographs of nanotubes grown at different  $C_2H_2:NH_3$  flow ratios. Note that the  $NH_3$  flow and the bias voltage were kept constant at 100 sccm and  $-600$  V, respectively, while the  $C_2H_2$  flow is varied. Furthermore, the pressure was also kept constant by adjusting the pumping speed in order to maintain similar plasma properties. Figures 12(a) and 12(b) show that well-aligned nanotubes with a uniform diameter can be grown for  $C_2H_2$  concentrations of 20% and 30%. Indeed, we find that nanotubes similar to those in Figs. 12(a) and 12(b) can be obtained for  $C_2H_2$  concentrations from 5% to 30%. Above 30%  $C_2H_2$ , the nanotubes become obelisk-like as seen in Fig. 12(c). For even higher  $C_2H_2$  flows the growth changes dramatically from nanotubes to tip structures, as in Fig. 12(d). A pure carbon plasma yields films resembling amorphous carbon, with a cauliflower-like structure often reported in the literature.<sup>30,31</sup>

Figure 11(c) plots the nanotube length against the  $C_2H_2$  concentration. As  $C_2H_2$  concentration increases, the growth rate initially rises by 30% and then decreases again. The initial rise in nanotube length is expected, as a higher concentration of feed gas in the plasma compensates for the etching by  $NH_3$ . The catalyst particles can be seen on top of all the structures, including the pyramids in Fig. 12(d). This indicates that, even at high  $C_2H_2$  flows, the carbon diffuses through the metal particles and precipitates below it. However, at concentrations over 50%, the vertical nanotube growth cannot keep pace with the amount of carbon extruded through the metal catalyst, so that the lateral growth below the metal cap dominates giving rise to pyramidal structures. Furthermore, since the relative amount of  $NH_3$  in the plasma is less, the etching rate is lower than the deposition rate, leading to a buildup of amorphous or poor quality carbon between the structures.

#### E. Influence of the deposition temperature

Nanotubes were grown at three different deposition temperatures while keeping all other parameters constant. Fig-

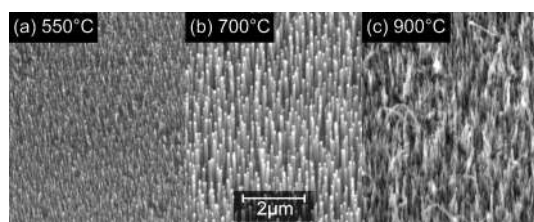


FIG. 13. SEM micrographs of nanotubes grown at (a) 550 °C, (b) 700 °C, and (c) 900 °C under standard conditions.

ures 13(a)–13(c) show the nanotubes grown at 550, 700 and 900 °C, respectively. The growth rate at 550 °C is much less, with the nanotubes having a diameter of 50 nm and a height of only 1 μm, similar to the results of Cui *et al.*<sup>19</sup> The results of Fig. 13(a) suggest that 550 °C may not be sufficient for nucleating nanotubes. However, this is not supported by HREM observations, which reveal short nanotubes with a bamboo-like structure (see below). The low growth rate appears to be a direct consequence of the low deposition temperature rather than a lack of plasma density, as thermal growth without a plasma occurs at 700 °C. At 550 °C, the temperature may be too low to decompose  $C_2H_2$ , hindering growth. Furthermore, the low temperature also limits the graphitization, which increases the condensation of *a*-C. The nanotubes grown at 700 °C are well-aligned and uniform in size. However, as the deposition temperature is further increased to about 900 °C, the nanotubes become disordered and less well aligned. The nanotube distortion at 900 °C may be caused by ion damage. At this temperature, the ion current is  $\approx 0.7$  A, indicating a higher plasma ionization.

Figure 14 shows the variation of growth rate with substrate temperature. It is seen that the growth rate initially increases with the substrate temperature and then decreases at higher temperatures. This trend is similar to that found by Cui *et al.*,<sup>19</sup> even though they used microwave PECVD in which ion bombardment effects are small. The trend is also quite similar to that in pyrolysis found by Baker,<sup>32–34</sup> which suggests a common mechanism, as discussed below.

## F. Transmission electron microscopy

The tubular structure of the nanotubes was verified using TEM. The nanotubes generally consisted of 20–30 graphitic

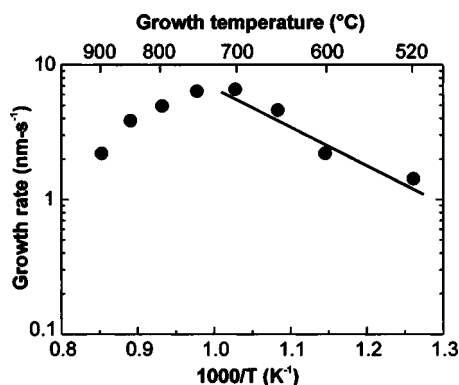


FIG. 14. Average nanotube length versus inverse deposition temperature.

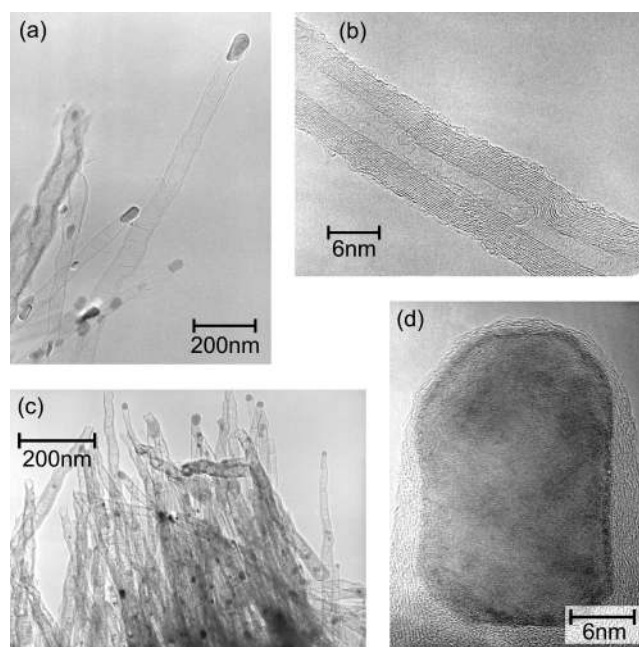


FIG. 15. Transmission electron microscopy images of (a) nanotubes deposited at 550 °C, (b) 700 °C and (c) 900 °C. (d) is a high magnification image of a catalyst particle from the 900 °C material.

shells with a central hollow region of about 3–5 nm. The Ni catalyst particle is always found at the top of the nanotubes. The HREM images reveal that the catalyst particle is mostly single crystal Ni completely encapsulated by carbon. Figures 15(a) and 15(c) show TEM images of nanotubes deposited using standard conditions but at substrate temperatures of 550 and 900 °C, respectively. The low and high temperature nanotubes have a more defective, bamboo-like structure, in contrast to nanotubes deposited at 700 °C as shown in Fig. 15(b). Their tube walls are also thinner ( $\approx 2$  to 3 nm). The smaller number of tube walls is consistent with a lower growth rate. The interrupted growth for the 550 and 900 °C nanotubes may be related to nonequilibrium extrusion of carbon from the catalyst particle. Examination of the tube walls reveal that the graphene planes were not always parallel to the tube axis but often twisted and broken for low temperature depositions while the graphite layers were found to be more defined for the high temperature case. The high resolution TEM image shown in Fig. 15(b) confirms the tubular nature of these nanotubes. Well-defined graphene planes parallel to the tube axis are clearly visible in Fig. 15(b). A similar structure along with defects in the form of “cross-struts” perpendicular to the tube axis are present in all PECVD grown nanotubes.

A high magnification image of the catalyst particle for the 900 °C nanotubes is shown in Fig. 15(d). Carbon encapsulation and the Ni fringes at the center of the particle can be readily observed. Note that the carbon surrounding the catalyst particle is graphitic in nature in this case due to the high deposition temperature. In contrast, the carbon layer surrounding the catalyst particles in the low temperature depositions was found to resemble disordered carbon.

Closer observation of Fig. 15(d) reveals three distinct regions in the image. The first is the Ni core of the catalyst



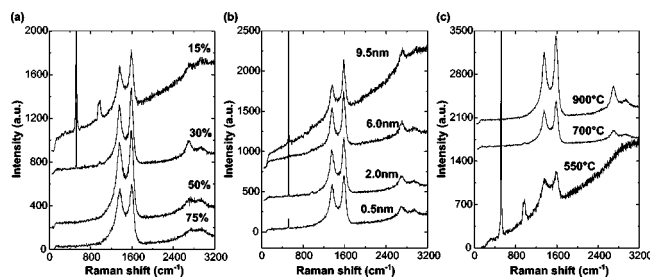


FIG. 16. Visible Raman spectra of nanotubes grown on (a) varying C<sub>2</sub>H<sub>2</sub>:NH<sub>3</sub> ratios, (b) different Ni thicknesses, and (c) varying deposition temperatures.

particle (consistent with fringe spacing of cubic Ni), the second is a shadowy interface region between the Ni particle and the carbon, and the third is the carbon encapsulation. The image indicates that carbon and Ni interact only near the edges of the catalyst and not with the entire particle. The spacing in the interface region appears to differ from that of pure Ni or graphite. The graphite phase also seems to be extruded outwards from this transition region. This appears to occur over the entire particle, consistent with the cap being completely encapsulated in three dimensions. Further work on the nature of the transition region will be reported elsewhere.

### G. Raman spectroscopy

Raman spectroscopy is a useful nondestructive method for the structural characterization of different carbon materials.<sup>35–37</sup> Most work on nanotubes has been performed on very pure SWNTs samples to determine their Raman signatures and correlate them to calculations.<sup>38–40</sup> In our case the samples contain some Ni and amorphous impurities which dilutes the nanotube signature. Nevertheless, structural information can still be extracted. Figure 16(a) shows the Raman spectra from nanotubes grown at varying C<sub>2</sub>H<sub>2</sub>:NH<sub>3</sub> ratios. The two main features in the Raman spectra are the *D* and *G* peaks at about 1350 and 1600 cm<sup>-1</sup> and the corresponding second order peaks at around 2700 and 2950 cm<sup>-1</sup>. The first and second order Si peaks are also seen. The 15% spectrum shows some photoluminescence (PL) background along with the second order Si peak at 960 cm<sup>-1</sup>, both consistent with the low growth rate of nanotubes at this concentration, Fig. 11(c). The second order *D* and *G* peaks become less prominent and the *I*(*D*)/*I*(*G*) ratio increases for higher C<sub>2</sub>H<sub>2</sub> concentrations.

The Raman spectra of nanotubes shown in Fig. 4 are plotted in Fig. 16(b). Again, there are no significant differences among the spectra. However, the nanotubes grown on a 9.5 nm Ni layer show a large photoluminescence (PL) background, attributed to the a-C between the short and less densely packed nanotubes. Figure 16(c) shows the Raman spectra of nanotubes grown at 550, 700 and 900 °C. The high temperature tubes have sharper *D* and *G* peaks, while the strong PL and the lack of second order *D* and *G* peaks in 550 °C spectrum indicates disordered tubes and the presence of large amounts of a-C. In general, we find that more aligned and ordered samples correspond to lower *I*(*D*)/*I*(*G*)

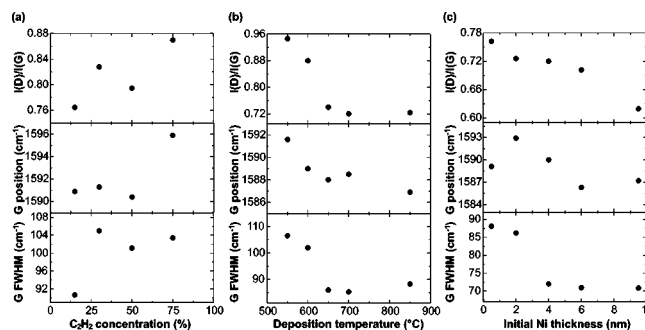


FIG. 17. Variation of Raman *G* peak, *I*(*D*)/*I*(*G*) ratio, and *G* peak width vs (a) acetylene concentration, (b) deposition temperature, and (c) Ni layer thickness.

ratios and sharper first and second order *D* and *G* peaks. The effects of acetylene concentration, deposition temperature, and catalyst layer thickness on the Raman spectrum parameters are summarized in Figs. 17(a)–17(c), respectively.

The visible and UV Raman spectra from the nanotubes grown at 700 °C are compared in Fig. 18. The UV Raman spectrum shows only a very sharp *G* peak. The absence of a residual *D* peak is consistent with ordered graphitic bonding within the tubes.<sup>35</sup>

### H. Auger analysis

A chemical analysis of the nanotube base, body, and tip was conducted using nano-Auger spectroscopy. By using a focused electron beam nanoprobe, the various portions of the nanotube were analyzed. Figure 19(a) shows the Auger chemical analysis from different regions of the nanotubes (deposited using standard conditions and 700 °C). The results show that the body of the nanotube is almost entirely carbon with only residual nitrogen and oxygen present in the form of adsorbed contaminants. Ni was never detected in the body of the nanotube for all our measurements. Ni catalyst together with carbon was readily detected at the top of the nanotube.

The nature of the carbon in the body and tip of the nanotube was derived from the Auger carbon signal. The carbon peak is shown in detail in Fig. 19(b). The prepeak feature from 260 to 270 eV for both the tip and the body of the nanotube indicates that carbon is predominantly *sp*<sup>2</sup> bonded. The better-defined features (crystalline graphite-like) of the spectrum from the body of the nanotube suggests that there

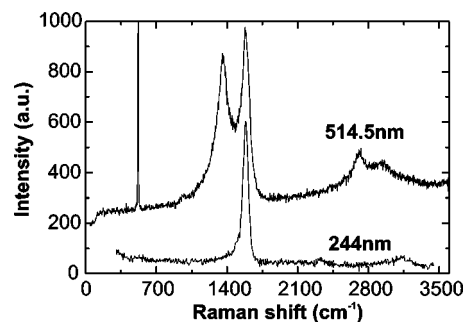


FIG. 18. UV and visible Raman spectra of nanotubes deposited at 700 °C.

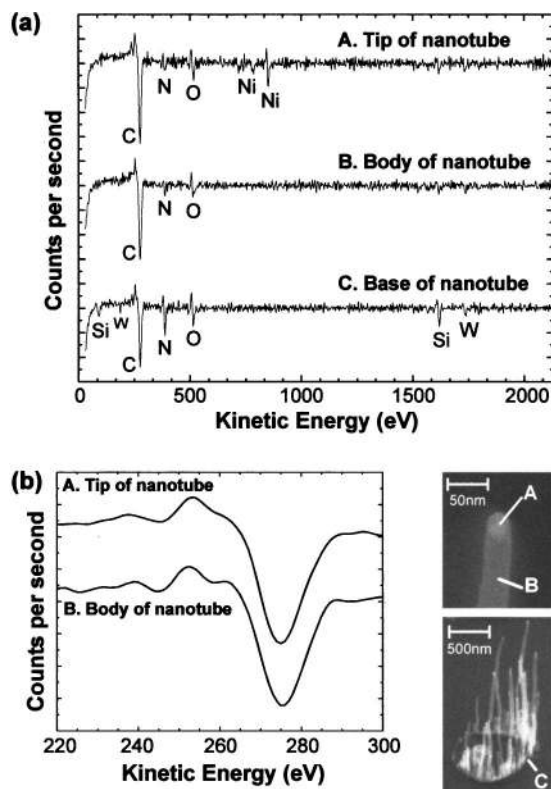


FIG. 19. Nano-Auger spectroscopy image and chemical analysis of the (a) tip, body, and base of a nanotube. The incorporation of W is expected to occur during Ni evaporation as a W boat is used or from the W elements embedded into the graphite heater. (b) Images of regions where the Auger analysis was performed and expanded energy region of the carbon peak showing that the material encapsulating the catalyst particle is a mixture of graphite and amorphous carbon (*a-C*) while the body of the nanotube is graphitic.

is a higher degree of crystallinity in the body, whereas the tip contains a mixture of both graphitic and amorphous  $sp^2$  carbon.

The spectrum of the nanotube base is very similar to that of the body. Surprisingly, no Ni was detected at the nanotube base. We also analyzed base regions where the nanotube was removed in order to detect any remnants of the catalyst particle, as shown in Fig. 19(a). Under no circumstances did we find any Ni at the base of the nanotubes, indicating that all the Ni is transported to the top, as diffusion into the substrate is limited by the  $\text{SiO}_2$  buffer layer. This strongly supports a growth model where the carbon is extruded through the catalyst. The growth of the nanotube in turn pushes the catalyst particle upwards.

#### IV. DISCUSSION

Our work suggests that aligned MWNTs grow by the generally accepted mechanism first proposed for filamentary carbon, shown in Fig. 20.<sup>32–34,40,41</sup> The carbonaceous gas decomposes on the surface of the catalyst particle, the carbon diffuses across the particle under an activity gradient, and the carbon then precipitates out on the opposite side. This basic tip-growth mechanism describes the growth of carbon whiskers and nanotubes on supported catalysts, in which the catalyst particle remains at the tip of the growing tube. A variant

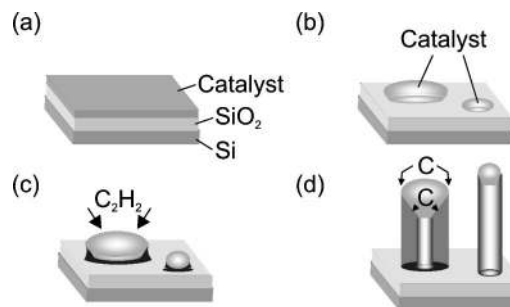


FIG. 20. Summary of the proposed growth mechanism of the nanotubes. (a) Si substrate with a thin  $\text{SiO}_2$  barrier layer and the Ni catalyst layer, (b) fragmentation of catalyst into nanoparticles by sintering, (c) decomposition of  $\text{C}_2\text{H}_2$  on the top surface of the Ni nanoparticle, and (d) growth of nanotubes below Ni catalyst by carbon diffusion through the Ni particle.

describes the base-growth situation. For catalyst particle sizes below a critical value, one nanotube grows per particle, with a diameter essentially equal to that of the particle. This equality was found in Fig. 6.

Figure 21 shows that the nanotube growth rate is roughly proportional to the inverse of the nanotube diameter. As the nanotube diameter is similar to the catalyst island size, the growth rate varies inversely with catalyst island size. This is as expected if the growth rate is controlled by diffusion across the catalyst particle.

Figure 14 showed the growth rate plotted against inverse temperature. An activation energy is derived from the low temperature leg and is found to be 0.56 eV. This is considerably less than that of carbon diffusion through Ni, about 1.5 eV.<sup>42</sup> This contrasts with carbon whisker growth by catalytic thermal decomposition, where the two activation energies were the same, and where the equality was used as good evidence for the carbon diffusion model.<sup>32–34</sup> The low activation energy for nanotube growth found for plasma growth is significant and may indicate a supersaturation of carbon in the metal. It suggests that room temperature growth may be possible through enhanced diffusion of carbon through the catalyst in PECVD growth.

These results suggest that the rate-limiting step is carbon diffusion across the catalyst, with a relatively low activation energy. In a few cases such as the catalytic pyrolysis of carbon monoxide or methane, the decomposition step is slow, but this is unlikely to be true in the PECVD situation. Thus the growth rate is maximized by minimizing the particle size, and the particle size controls both nanotube diameter and growth rate.

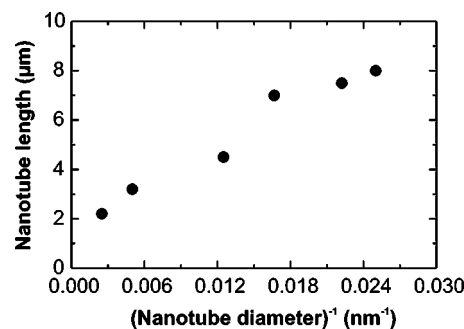


FIG. 21. Average nanotube length vs the inverse of the average nanotube diameter.



The catalyst particles are formed by sintering, due to nonwetting of the substrate. The particle size will depend on the initial film thickness, the underlying surface, and the anneal temperature. The temperature varies both the surface energies, but too high a temperature can allow larger islands to form due to Ostwald ripening. A higher anneal temperature can also encourage the formation of silicides which would anchor the catalyst and promote base growth.

Our SEM and TEM observations reveal that the catalyst particle on top of short nanotubes ( $\leq 1 \mu\text{m}$ ) grown on 2 nm Ni film is oval-shaped, while it is conical for longer nanotubes (several  $\mu\text{m}$ ). The catalyst particle for nanotubes grown on Ni film over 4 nm appear conical almost from the very start of growth, as seen in Fig. 4(f). The results suggest that for thin Ni films ( $\leq 2 \text{ nm}$ ), the nanotube growth process causes the change in the shape of the catalyst particle. On the other hand, for thick Ni films the Ni droplets are larger after annealing (Fig. 1) so the contact area with the substrate is also greater and therefore the adhesion between the Ni with the substrate is stronger. As the nanotube growth is initiated on the larger Ni droplets, the force required to detach them from the substrate is higher than that required for smaller Ni particles. This mechanical pulling of the larger Ni particles could be the origin of the observed conical shape.

The smaller Ni droplets obtained from thin Ni films have a small contact area so they are easily detached from the substrate. The smaller Ni particles maintain their shape during the initial part of nanotube growth but then become conical. The change in shape is most probably related to the dissolution, precipitation, and saturation of carbon into the Ni. The bottom part of the particle is then preferentially eroded during the catalysis process, giving it the conical shape. Further evidence of this type of growth mechanism is that the base of the nanotubes was always found to have a slightly larger diameter than the top, indicating that a change in the size and shape of the catalyst particle is occurring.

The function of  $\text{NH}_3$  is to etch the competing amorphous carbon and graphitic phases. It may also have a role in keeping the gas side of the catalyst particle free of carbon, to allow continuing access of gas to the catalyst, and prevent it from becoming deactivated. The comparative behavior of various etching gases, ammonia, and hydrogen is presently being studied.

## V. CONCLUSIONS

The process conditions for the growth of vertically aligned carbon nanotubes by dc PECVD was studied in detail as a function of the Ni catalyst layer thickness, bias voltage, deposition temperature,  $\text{C}_2\text{H}_2:\text{NH}_3$  ratio, and pressure. An annealing step causes the catalyst layer to fragment into islands of size proportional to its initial thickness. The island size controls the subsequent nanotube diameter, growth rate, and areal density of the nanotubes. The alignment of the nanotubes depends on the electric field. The growth rate varies inversely with the nanotube diameter and passes through a maximum as a function of growth temperature. Our results indicate that nanotube growth occurs by diffusion of carbon

through the Ni catalyst particle, which rides on the nanotube tip. The activation energy for growth is, however, less than previously reported carbon diffusion in Ni.

## ACKNOWLEDGMENTS

The authors would like to thank V A Tech Reyorle, UK for funding the nanotube growth project. K. B. K. T. acknowledges support from the Association of Commonwealth Universities and the British Council. The help of G. Pirio, P. Legagneux, F. Wycisk, J. Olivier, and D. Pribat from Thales in the Auger measurements is also acknowledged. C. D. acknowledges the EU CARBEN project for funding.

- <sup>1</sup>R. H. Baughman, C. X. Cui, A. A. Zakhidov, Z. Iqbal, J. N. Barisci, G. M. Spinks, G. G. Wallace, A. Mazzoldi, D. De Rossi, A. G. Rinzler, O. Jachinski, S. Roth, and M. Kertesz, *Science* **284**, 1340 (1999).
- <sup>2</sup>A. C. Dillon, K. M. Jones, T. A. Bekkedahl, C. H. Kiang, D. S. Bethune, and M. J. Heben, *Nature (London)* **386**, 377 (1997).
- <sup>3</sup>B. Gao, A. Kleinhammes, X. P. Tang, C. Bower, L. Fleming, Y. Wu, and O. Zhou, *Chem. Phys. Lett.* **307**, 153 (1999).
- <sup>4</sup>C. M. Niu, E. K. Sichel, R. Hoch, D. Moy, and H. Tennent, *Appl. Phys. Lett.* **70**, 1480 (1997).
- <sup>5</sup>J. N. Barisci, G. G. Wallace, and R. H. Baughman, *J. Electroanal. Chem.* **488**, 92 (2000).
- <sup>6</sup>E. Frackowiak, K. Metenier, V. Bertagna, and F. Beguin, *Appl. Phys. Lett.* **77**, 2421 (2000).
- <sup>7</sup>S. Ijima, *Nature (London)* **354**, 56 (1991).
- <sup>8</sup>S. Ijima and T. Ichihashi, *Nature (London)* **363**, 603 (1993).
- <sup>9</sup>C. Journet, W. K. Maser, P. Bernier, A. Loiseau, M. L. delaChappelle, S. Lefrant, P. Deniard, R. Lee, and J. E. Fischer, *Nature (London)* **388**, 756 (1997).
- <sup>10</sup>A. Thess, R. Lee, P. Nikolaev, H. J. Dai, P. Petit, J. Robert, C. H. Xu, Y. H. Lee, S. G. Kim, A. G. Rinzler, D. T. Colbert, G. E. Scuseria, D. Tomanek, and J. E. Fischer, *R. E. Smalley, Science* **273**, 483 (1996).
- <sup>11</sup>C. Journet, and P. Bernier *Appl. Phys. A: Mater. Sci. Process.* **67**, 1 (1998).
- <sup>12</sup>A. M. Cassell, J. A. Raymakers, J. Kong, and H. J. Dai, *J. Phys. Chem.* **103**, 6484 (1999).
- <sup>13</sup>W. Z. Li, S. S. Xie, L. X. Qian, B. H. Chang, B. S. Zou, W. Y. Zhou, R. A. Zhao, and G. Wang, *Science* **274**, 1701 (1996).
- <sup>14</sup>Z. F. Ren, Z. P. Huang, J. W. Xu, J. H. Wang, P. Bush, M. P. Siegal, and P. N. Provencio, *Science* **282**, 1105 (1998).
- <sup>15</sup>S. S. Fan, M. G. Chapline, N. R. Franklin, T. W. Tombler, A. M. Cassell, and H. J. Dai, *Science* **283**, 512 (1999).
- <sup>16</sup>C. Bower, O. Zhou, W. Zhu, D. J. Werder, and S. Jin, *Appl. Phys. Lett.* **77**, 2767 (2000).
- <sup>17</sup>V. I. Merkulov, D. H. Lowndes, Y. Y. Wei, G. Eres, and E. Voelkl, *Appl. Phys. Lett.* **76**, 3555 (2000).
- <sup>18</sup>R. Andrews, D. Jacques, A. M. Rao, F. Derbyshire, D. Qian, X. Fan, E. C. Dickey, and J. Chen, *Chem. Phys. Lett.* **303**, 467 (1999).
- <sup>19</sup>H. Cui, O. Zhou, and B. R. Stoner, *J. Appl. Phys.* **88**, 6072 (2000).
- <sup>20</sup>F. Hoshi, K. Tsugawa, A. Goto, T. Ishikura, S. Yamashita, M. Yumura, T. Hirao, K. Oura, and Y. Koga, *Proceedings of the Specialist Meeting on Amorphous Carbon (SMAC)*, Torino, Italy, 2001.
- <sup>21</sup>W. A. de Heer, A. Chatelaine, and D. Ugarte, *Science* **270**, 1179 (1995).
- <sup>22</sup>J. M. Bonard, J. P. Salvetat, T. Stockli, L. Forro, and A. Chatelain, *Appl. Phys. A: Mater. Sci. Process.* **69**, 245 (1999).
- <sup>23</sup>J. M. Kim, W. B. Choi, N. S. Lee, and J. E. Jung, *Diamond Relat. Mater.* **9**, 1184 (2000).
- <sup>24</sup>W. Zhu, C. Bower, O. Zhou, G. Kochanski, S. Jin, *Appl. Phys. Lett.* **75**, 873 (1999).
- <sup>25</sup>P. G. Collins and A. Zettl, *Appl. Phys. Lett.* **69**, 1969 (1996).
- <sup>26</sup>K. Ryu, M. Kang, Y. Kim, and H. Jeon, *Thin Solid Films* (to be published).
- <sup>27</sup>Z. P. Huang, J. W. Wu, Z. F. Ren, J. H. Wang, M. P. Siegal, and P. N. Provencio, *Appl. Phys. Lett.* **73**, 3845 (1998).
- <sup>28</sup>M. A. Lieberman and A. J. Lichtenberg, *Principles of Plasma Discharges and Materials Processing* (Wiley, New York, 1999).
- <sup>29</sup>C. Bower, W. Zhu, S. Jin, and O. Zhou, *Appl. Phys. Lett.* **77**, 830 (2000).
- <sup>30</sup>B. S. Satyanarayana, J. Robertson, W. I. Milne, *J. Appl. Phys.* **87**, 3126 (2000).

- <sup>31</sup>A. C. Ferrari, and J. Robertson, *Phys. Rev. B* **61**, 14095 (2000).
- <sup>32</sup>R. T. K. Baker, M. A. Barber, F. S. Feates, P. S. Harris, and R. J. Waite, *J. Catal.* **26**, 51 (1972).
- <sup>33</sup>R. T. K. Baker, P. S. Harris, R. B. Thomas, R. J. Waite, *J. Catal.* **30**, 86 (1973).
- <sup>34</sup>R. T. K. Baker and P. S. Harris, in *Chemistry and Physics of Carbon* edited by P. L. Walker and P. A. Thrower (Dekker, New York, 1978), Vol 14, p. 83.
- <sup>35</sup>M. S. Dresselhaus and P. C. Eklund, *Adv. Phys.* **49**, 705 (2000).
- <sup>36</sup>A. M. Rao, A. Jorio, M. A. Pimenta, M. S. S. Dantas, R. Saito, G. Dresselhaus, and M. S. Dresselhaus, *Phys. Rev. Lett.* **84**, 1820 (2000).
- <sup>37</sup>A. M. Rao, E. Richter, S. Bandow, B. Chase, P. C. Eklund, K. A. Williams, S. Fang, K. R. Subbaswamy, M. Menon, A. Thess, R. E. Smalley, G. Dresselhaus, and M. S. Dresselhaus, *Science* **275**, 187 (1997).
- <sup>38</sup>R. Saito, T. Takeya, T. Kimura, G. Dresselhaus, and M. S. Dresselhaus, *Phys. Rev. B* **57**, 4145 (1998).
- <sup>39</sup>G. S. Duesberg, I. Loa, M. Burghard, K. Syassen, and S. Roth, *Phys. Rev. Lett.* **85**, 5436 (2000).
- <sup>40</sup>G. G. Tibbetts, *J. Cryst. Growth* **66**, 632 (1984).
- <sup>41</sup>H. Kanzow, A. Ding, *Phys. Rev. B* **60**, 11180 (1999).
- <sup>42</sup>R. P. Smith, *Trans. Metall. Soc. AIME* **236**, 1224 (1966).